

Dilatancy and compaction in a pressure control granular system under an oscillatory shear

Daisuke Ishima and Hisao Hayakawa

Yukawa Institute for Theoretical Physics, Kyoto University, Kyoto 606-8502, Japan

(Dated: February 14, 2019)

We numerically study the rheology of a frictional granular system confined by a constant pressure under an oscillatory shear. We find several scaling laws for the storage and the loss moduli against the scaled strain amplitude. These scaling laws can be understood by the angular distribution of the contact force. The system exhibits the dilatancy for the large strain amplitudes, while the system can be compactified for the middle strain amplitudes if the pressure is small. The rheological change between the jammed phase and the compaction phase or between the jammed phase and the dilatancy phase or the compaction phase and the dilatancy phase can be detected by the peak of the stress anisotropy.

INTRODUCTION

Amorphous materials consisting of dissipative grains such as powders [1], colloid suspensions [2], bubbles [3] and emulsions exhibit jamming transitions from liquid-like states to solid-like jammed states. Since the pioneer work by Liu and Nagel [4], studies on the jamming transition have attracted much attention among physicists. The jamming transition is known as a mixed transition in which the coordination number is discontinuously changed while the pressure and the shear stress are continuously changed at the jamming point for frictionless systems [5]. Such a continuous change of the stress near the jamming point can be described by scaling laws among the pressure, the shear stress, the shear rate and the density [5–11].

It is remarkable that the introduction of mutual frictions between grains drastically changes the behavior of the jamming transition including the existence of a discontinuous shear thickening (DST) and the discontinuous change of the stress [12–17]. Recently, we have recognized that a shear jammed state commonly observed in frictional systems induced by a shear differs from the conventional jammed state [18–24]. Many people are interested in the mutual relationship between the shear jamming and the DST, but it seems that we do not have any consensus for the relationship [25, 26].

Unlike the picture of the jamming transition, there is another important rheological transition from an elastic response to a plastic response by applying external forces, which is referred to as the yielding transition [27–29]. It corresponds to the reversible-irreversible transition i.e. the position of a tracer grain can return its original position for the small shear while its position does not return the original one for the large shear [27, 30]. The steady state in a simple shear is always plastic above the yielding point, where the critical behavior near the yielding point can be described by a scaling theory [29, 31]. Various definitions of the yielding point exists for oscillatory shears, but each of them is not equivalent [32].

The dilatancy is widely known as one of typical characteristics of granular systems in which the density de-

creases as the shear increases under a constant pressure condition [33–37]. Because the dilatancy cannot be observed in a constant volume system, we have to study the rheology of granular systems confined by a constant pressure under the oscillatory shear to know the details of the dilatancy.

The purpose of this paper is to know rheological properties of a sheared granular system such as the yielding transition and the dilatancy. For this purpose, we numerically study a granular system confined by a constant pressure under oscillatory shear.

The contents of this paper is as follows. In the next section we explain the setup of our numerical simulation. The results of our simulation are explained in Secs. III and IV. In Sec. III, we demonstrate the existence of several scaling laws for the storage and the loss moduli, which are essentially understood by the angular distribution of contact force. In Sec. IV, we draw the phase diagram for our system on the plane of the volume fraction and the strain amplitude to illustrate the existence of the dilatancy and the compaction. In the last section, we discuss and summarize our results. In Appendices, we explain some technical details which have not been mentioned in the main text.

OUR SIMULATED SYSTEM

Let us explain the setup of our simulated system. We consider a two-dimensional system consisting of N frictional granular disks in which the numbers of grains for the diameters d_0 , $0.9d_0$, $0.8d_0$, and $0.7d_0$ are $N/4$, respectively, to prevent the system from crystallization [38]. We assume that the density of each grain is a constant and the mass is proportional to the square of the diameter of the grain. Then, the mass corresponding to the largest diameter d_0 is m_0 .

We assume that the gravity does not play any role in our system corresponding to grains on smooth horizontal plane. We impose the periodic boundary condition in x -direction, while we apply the external pressure through the real boundary in y -direction. The shape of

the system is a square, i.e. $L_y = L_x$ in the absence of any external pressure, where L_x and L_y are the linear dimensions of x - and y -directions, respectively. When the external pressure is applied, $L_y(t)$ depends on time. The boundary at $y = L_y(t)/2$ obeys $A \sin(\Omega t)$ where A and Ω are the strain amplitude and the angular frequency, respectively. Because the linear dimension of the system size in the y -direction is not constant, we introduce the effective strain amplitude $\gamma_{0,\text{eff}} := 2A/L_x$ as the control parameter.

We average the data over N_T cycles after abandon the data in the initial N_{ini} cycles. Because the obtained results depend on N_{ini} for $N_{\text{ini}} \leq 5$, we adopt $N_{\text{ini}} = 10$ and $N_T = 10$. We set $t = 0$ at the moment when N_{ini} oscillatory shear ends. We control the pressure on the wall. To

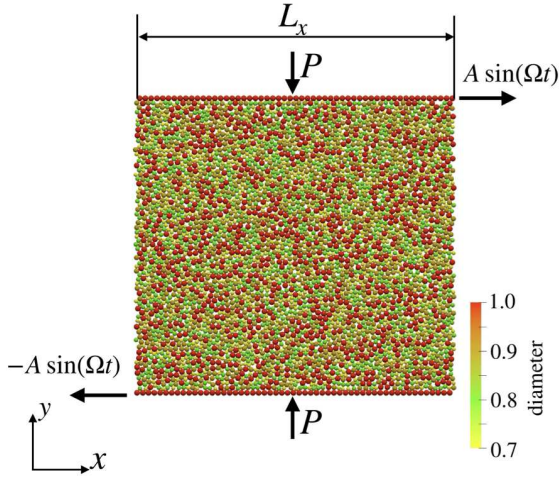


FIG. 1. A snapshot of our simulated system, where P , A and Ω are the external pressure, the strain amplitude and the angular frequency of the external oscillation, respectively.

describe the motion of the walls at $y = \pm L_y(t)/2$ under the external pressure P , we adopt the following equation of the motion:

$$m_w \frac{dv_{w,y}^{\pm}}{dt} = \pm(P_w^{\pm} - P)L_x - \zeta_d v_{w,y}^{\pm}, \quad (1)$$

where m_w , $v_{w,y}^{\pm}$, P_w^{\pm} and ζ_d are the mass of the wall, y -component velocities of the wall located at $\pm L_y(t)/2$, the inner pressure acting on the walls from grains, and the damping constant, respectively. Each wall consists of N_w grains of mass m_0 and diameter d_0 , in which N_w satisfies $m_w = N_w m_0$.

The translational and the rotational equations of the motion of the i -th grain whose mass, position, and moment of inertia are, respectively, m_i , \mathbf{x}_i , and I_i are given by

$$m_i \frac{d^2 \mathbf{x}_i}{dt^2} = \sum_{j \neq i} \mathbf{f}_{ij}, \quad (2)$$

$$I_i \frac{d\omega_i}{dt} = \sum_{j \neq i} T_{ij}, \quad (3)$$

where we have introduced the contact force \mathbf{f}_{ij} acting on the i -th grain from j -th grain. Note that ω_i is z -component of the angular velocity of the i -th grain. The definition of the torque T_{ij} in Eq. (3) is given by

$$T_{ij} = -\frac{d_i}{2} \mathbf{f}_{ij} \cdot \mathbf{t}_{ij} \quad (4)$$

with the tangential unit vector \mathbf{t}_{ij} at the contact point between i -th and j -th grains. The contact force of each grain is described by the Cundall-Stack model [39, 40]. Let us consider the contact force \mathbf{f}_{ij} between i -th and j -th grains. Introducing $r_{ij} = (d_i + d_j)/2$ and $\mathbf{x}_{ij} = \mathbf{x}_i - \mathbf{x}_j$ with $x_{ij} := |\mathbf{x}_{ij}|$, the contact force \mathbf{f}_{ij} is expressed as

$$\mathbf{f}_{ij} = (\mathbf{f}_{ij,n} + \mathbf{f}_{ij,t}) \Theta(r_{ij} - x_{ij}), \quad (5)$$

where we have introduced the normal contact force $\mathbf{f}_{ij,n}$, the tangential contact force $\mathbf{f}_{ij,t}$ and Heaviside's step function $\Theta(x)$ satisfying $\Theta(x) = 1$ for $x \geq 0$ and $\Theta(x) = 0$ otherwise. The normal force consists of the elastic repulsive force represented by a linear spring (the spring constant k_n) and the dissipative force represented by a dash pot (the damping constant η_n) as

$$\mathbf{f}_{ij,n} = k_n \delta_{ij,n} \mathbf{n}_{ij} - \eta_n \mathbf{v}_{ij,n}, \quad (6)$$

where we have introduced $\mathbf{n}_{ij} = \mathbf{x}_{ij}/x_{ij}$, $\mathbf{v}_{ij,n} = (\mathbf{v}_{ij} \cdot \mathbf{n}_{ij}) \mathbf{n}_{ij}$ with $\mathbf{v}_{ij} = d\mathbf{x}_{ij}/dt$ and $\delta_{ij,n} = r_{ij} - x_{ij}$. On the other hand, the tangential force $\mathbf{f}_{ij,t}$ contains both a sticking state and a slip state, where the switching from the stick to the slip takes place if the magnitude of tangential force $f_{ij,t} = |\mathbf{f}_{ij,t}|$ exceeds the critical condition as

$$\mathbf{f}_{ij,t} = \begin{cases} k_t \delta_{ij,t} \mathbf{t}_{ij} - \eta_t \mathbf{v}_{ij,t} & (f_{ij,t} < \mu f_{ij,n}), \\ \mu f_{ij,n} \mathbf{t}_{ij} & (\text{otherwise}), \end{cases} \quad (7)$$

where $\delta_{ij,t}$ is the tangential displacement during a contact time and we have introduced Coulomb's friction constant μ , the tangential spring constant k_t , the tangential damping constant η_t , $f_{ij,n} = |\mathbf{f}_{ij,n}|$ and the relative tangential velocity at the contact point $\mathbf{v}_{ij,t} = \mathbf{v}_{ij} - \mathbf{v}_{ij,n} + (d_i \omega_i + d_j \omega_j)/2$.

The parameters of our system are listed in Tables 1 and 2. In the most of our simulations we adopt the number of grains $N = 4000$, the friction coefficient $\mu = 1.0$, and the frequency $\Omega/(2\pi) = 1.0 \times 10^{-4} \sqrt{k_n/m_0}$. We have confirmed that the rigidity and the viscosity are independent of Ω in the range of $\Omega/(2\pi) \leq 1.0 \times 10^{-4} \sqrt{k_n/m_0}$ (see Appendix).

TABLE I. List of the system parameters, where $\hat{\zeta}_d$ and $\hat{\eta}_n$ are $\hat{\zeta}_d := \zeta_d/\sqrt{m_0 k_n}$ and $\hat{\eta}_n := \eta_n/\sqrt{m_0 k_n}$, respectively.

N	L_x/d_0	$\hat{\zeta}_d$	μ	k_t/k_n	$\hat{\eta}_n$	η_t/η_n
4000 ~ 20000	50 ~ 100	1	0 ~ 1.0	0.5	1	1

TABLE II. List of the external parameters.

$\gamma_{0,\text{eff}}$	$\Omega/(2\pi\sqrt{k_n/m_0})$	P/k_n
$10^{-6} \sim 1$	$10^{-5} \sim 10^{-3}$	$2.0 \times 10^{-5} \sim 6.0 \times 10^{-3}$

In order to make the initial configuration isotropic, we randomly place all grains whose diameters are $0.6d_0$ confined in a squared system without shear. When the potential energy $V_n := k_n \sum_{i \neq j} \delta_{ij,n}^2$ satisfies $V_n/(Nk_n d_0^2) < 1.0 \times 10^{-7}$, the diameter of each grain increases by $0.02d_0$. After repeating this process we reach the designed diameter of each grain at the below jamming density. We give each grain a uniform random velocity in the range between $-0.01d_0\sqrt{k_n/m_0}$ and $0.01d_0\sqrt{k_n/m_0}$ for the whole grains to eliminate unexpected unstable structure. We compress both walls by the pressure P to compactify the system above the jamming density. After the sufficient time (elapsed time = $1.5 \times 10^5 \sqrt{m_0/k_n}$), all the velocities and the rotational velocities are set to zero to obtain isotropic and stable structure as the initial condition. Then, we apply the oscillatory shear. We adopt the symplectic Euler method with time the time step $\Delta t = 0.05\sqrt{m_0/k_n}$.

To avoid the influence of shear band effects we only collect the data in the bulk region which is apart from the walls by the distance $7d_0$. The velocity profile in the bulk region is almost linear for large strains.

Because the contact stress is dominant for dense granular systems [41, 42], we measure the symmetric contact stress $\sigma_{\alpha\beta}^{\text{sym}}$:

$$\sigma_{\alpha\beta}^{\text{sym}} := -\frac{1}{2L_x \tilde{L}_y} \sum_{\substack{i \\ (|y_i| < \tilde{L}_y/2)}} \sum_{j>i} (x_{ij,\alpha} f_{ij,\beta} + x_{ij,\beta} f_{ij,\alpha}), \quad (8)$$

where we have introduced $\tilde{L}_y = L_y(t = -2N_{\text{ini}}\pi/\Omega) - 14d_0$. Note that frictional systems have asymmetric stress tensor and the coupled stress in general [43]. Nevertheless, we have confirmed that the asymmetry of the stress tensor is so small that we can ignore the asymmetry of the stress tensor or the coupled stress (see Appendix).

In systems under the oscillatory shear, the storage modulus G' and the loss modulus G'' express the rigidity and the dynamic viscosity multiplied by Ω , respectively. It should be noted that their definitions are not unique in nonlinear response regime [44–46]. In this paper, we adopt the following expressions [46]:

$$G'(\gamma_{0,\text{eff}}, P) := \lim_{\gamma \rightarrow \gamma_{0,\text{eff}}} \frac{\tilde{\sigma}}{\gamma_{0,\text{eff}}}, \quad (9)$$

$$G''(\gamma_{0,\text{eff}}, P) := \lim_{\gamma \rightarrow 0 (\tilde{\sigma} \geq 0)} \frac{\tilde{\sigma}}{\gamma_{0,\text{eff}}}, \quad (10)$$

where we have introduced $\tilde{\sigma}$

$$\tilde{\sigma}(t) := \sigma_{xy}^{\text{sym}}(t) - \overline{\sigma_{xy}^{\text{sym}}}. \quad (11)$$

Here $\overline{\sigma_{xy}^{\text{sym}}}$ is the time average over the oscillatory period $\overline{\sigma_{xy}^{\text{sym}}} := \int_0^T dt \sigma_{xy}^{\text{sym}}/T$.

To specify the yielding point we check whether tracer grains return to their original positions after one cycle of the oscillatory shear (see Fig. 2). If the mean square displacement (MSD) parallel to shear is larger than the threshold $1.0 \times 10^{-6}d_0^2$, we regard the system as a plastic state. Here, MSD is evaluated by $\Delta x^2 := \sum_{n=1}^{N_T-1} \Delta x_{n,\text{raw}}^2 / (N_T - 1)$ where $\Delta x_{n,\text{raw}}^2$ is defined by

$$\Delta x_{n,\text{raw}}^2 := \frac{\sum_{\substack{i \\ (|y_i| < \tilde{L}_y/2)}} \{x_i(nT) - x_i((n-1)T)\}^2}{N_B((n-1)T)}, \quad (12)$$

where T is the oscillation period $T := 2\pi/\Omega$. Here, $N_B(t)$ and $x_i(t)$ are the number of grains in the bulk region and x coordinates of i -th grain at time t , respectively. Note that Eq. (12) does not contain any average on the phase of oscillation.

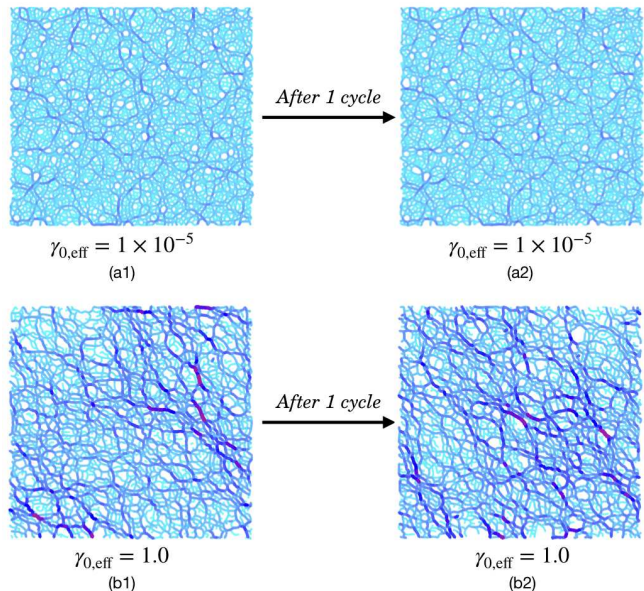


FIG. 2. The changes of force chains after one cycle at $P/k_n = 2.0 \times 10^{-3}$ and $N = 4000$ for $\gamma_{0,\text{eff}} = 1.0 \times 10^{-5}$ and $\gamma_{0,\text{eff}} = 1.0$. The line width of each line is proportional to the absolute value of the contact force between grains.

SCALING LAWS AND FRICTION DEPENDENCE

Scaling laws for storage and loss moduli

In this subsection we illustrate the existence of several scaling laws for the storage and the loss moduli. We also demonstrate that the stress-strain curve observed in our simulation can be reproduced by a phenomenology with the aid of the data of the angular distribution of

the contact force. We confirm that the following scaling form for the storage modulus holds (see Fig. 3):

$$G' = G'_{\text{res}}(\hat{P}) \mathcal{G}' \left(\frac{\gamma_{0,\text{eff}}}{\hat{P}^{\beta'_1}} \right), \quad (13)$$

$$G'_{\text{res}}(\hat{P}) := \lim_{\gamma_{0,\text{eff}} \searrow 0} G'(\gamma_{0,\text{eff}}, \hat{P}), \quad (14)$$

$$\lim_{x \searrow 0} \mathcal{G}'(x) = 1, \quad \lim_{x \rightarrow \infty} \mathcal{G}'(x) \sim x^{-1}, \quad (15)$$

where we have introduced $\hat{P} := P/k_n$ and the scaling exponent β'_1 which is a special case of μ -dependent exponent β'_μ . The exponent β'_1 is evaluated as

$$\beta'_1 = 1.06 \pm 0.04. \quad (16)$$

Note that the residual storage modulus $G'_{\text{res}}(\hat{P})$ has a

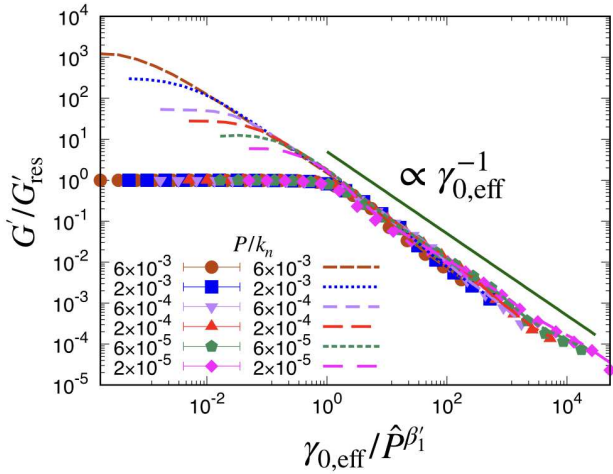


FIG. 3. Scaling plots of the storage modulus G'/G'_{res} for various dimensionless pressures \hat{P} against the scaled $\gamma_{0,\text{eff}}$, where G'_{res} is the residual storage modulus. Numerical storage modulus G' are plotted by filled symbols and the phenomenological storage modulus are plotted with lines. Here G' is proportional to $\gamma_{0,\text{eff}}^{-1}$ for large $\gamma_{0,\text{eff}}$.

weak pressure dependence as $G'_{\text{res}}/k_n \simeq a \ln \hat{P} + b$ with $a \simeq 0.03$ and $b \simeq 0.49$ (see Appendix). We also note that G'/G'_{res} is almost independent of $\gamma_{0,\text{eff}}$ for small $\gamma_{0,\text{eff}}$ and it is proportional to $\gamma_{0,\text{eff}}^{-1}$ for large $\gamma_{0,\text{eff}}$. The scaling exponent β'_1 approximately satisfies $\beta'_1 \approx 1$. The scaling behavior in Eqs. (13)-(16) can be understood as follows. If the strain is small, the response of the material is the Hookean in which G' must be independent of $\gamma_{0,\text{eff}}$. On the other hand, the stress ratio σ_{xy}/P approaches a constant for large strain regime. Thus, the effective stress $\tilde{\sigma}$ must be independent of $\gamma_{0,\text{eff}}$. This simple picture explains the basic mechanism of the scaling of G' .

The loss modulus also satisfies the scaling form (see Fig. 4):

$$G'' = k_n \hat{P}^{\alpha''_1} \mathcal{G}'' \left(\frac{\gamma_{0,\text{eff}}}{\hat{P}^{\beta''_1}} \right), \quad (17)$$

$$\lim_{x \searrow 0} \mathcal{G}''(x) = \text{const.}, \quad \lim_{x \rightarrow \infty} \mathcal{G}''(x) \sim x^{-1}, \quad (18)$$

where the scaling exponents α''_1 and β''_1 which are the special cases of α''_μ and β''_μ are evaluated as

$$\alpha''_1 = 0.17 \pm 0.02, \quad \beta''_1 = 0.94 \pm 0.02. \quad (19)$$

The exponent $\beta''_1 \approx 1$ can also be understood by the fact that the stress should be independent of $\gamma_{0,\text{eff}}$ or the stress ratio approaches a constant for large strain. The

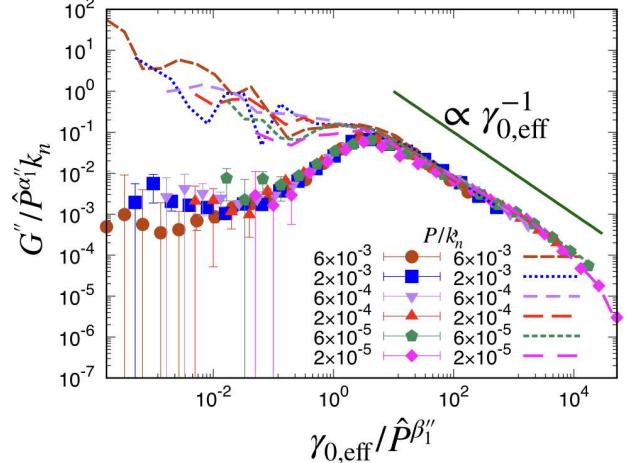


FIG. 4. Scaling plots of the loss modulus G'' for various dimensionless pressures \hat{P} against the scaled strain amplitude, where G'' is proportional to $\gamma_{0,\text{eff}}^{-1}$ for large $\gamma_{0,\text{eff}}$. Numerical loss modulus G'' are plotted by filled symbols and the phenomenological loss modulus are plotted with lines.

existence of a peak in the scaled loss modulus around at $\gamma_{0,\text{eff}}/\hat{P}^{\beta''_1}$ is characteristic. The loss modulus for small $\gamma_{0,\text{eff}}$ may not satisfy the scaling. On the other hand, the scaling function of G'' is also proportional to $\gamma_{0,\text{eff}}^{-1}$ for large $\gamma_{0,\text{eff}}$ as in the case of G' .

We may understand the qualitative behavior of G'' because of the balance between the creation and annihilation of the contact networks [47]. Namely, the energy loss is small if there are no bond breakages for small strain. Then, the energy loss increases as the strain increases for intermediate strain because of active reconnections of the contact network in this regime. Finally, the energy loss becomes smaller once the system contains some large slip layers.

Let us try to understand the behavior G' and G'' as well as the stress-strain curve quantitatively. In a system under a simple shear, it is known that the approximate stress tensor can be expressed with the aid of the angular distributions of the normal contact force density $\zeta_n(\theta)$ and tangential contact force density $\zeta_t(\theta)$ [42, 48–50]. Here $\zeta_n(\theta)$ and $\zeta_t(\theta)$ are expressed as $\zeta_n(\theta) = \rho(\theta)F_N(\theta)/\langle F_N \rangle$ and $\zeta_t(\theta) = \rho(\theta)F_T(\theta)/\langle F_N \rangle$ with the angular contact distribution $\rho(\theta)$ with the normalization $\int_0^{2\pi} d\theta \rho(\theta) = 1$, the normal force $F_N(\theta)$, the tangential force $F_T(\theta)$ at the contact angle θ , and the averaged contact force over the angle $\langle F_N \rangle = \int_0^{2\pi} d\theta \rho(\theta) F_N(\theta)$. From the normalization and the absence of global rotation

$\zeta_n(\theta)$ and $\zeta_t(\theta)$ satisfy $\int_0^{2\pi} d\theta \zeta_n(\theta) = 1$ and $\int_0^{2\pi} d\theta \zeta_t(\theta) = 0$, respectively. Figure 5 plots $\zeta_n(\theta)$ and $\zeta_t(\theta)$ in our system for various $\gamma_{0,\text{eff}}$. Basic behavior of $\zeta_n(\theta)$ or $\zeta_t(\theta)$ in our system is similar to that observed in a simple shear [42]. Nevertheless, the transition from isotropic $\zeta_n(\theta)$ for small strain amplitudes to anisotropic $\zeta_n(\theta)$ for large strain amplitudes is characteristic in oscillatory systems.

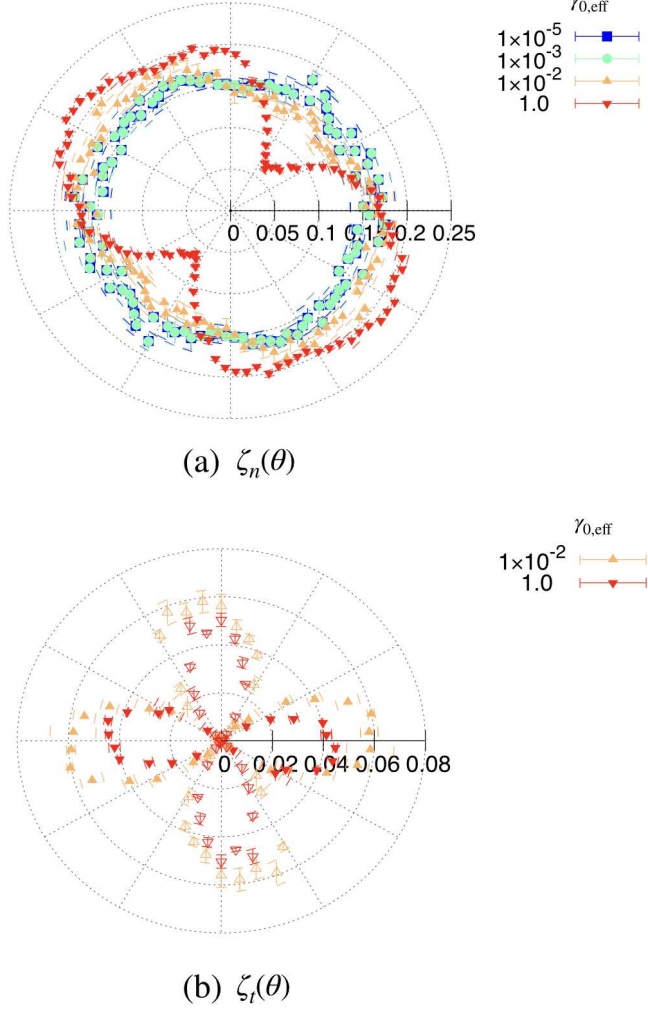


FIG. 5. Angular distributions for the normal contact force density $\zeta_n(\theta)$ (a) and the tangential contact force density $\zeta_t(\theta)$ at $\Omega t = 0$ (b). The tangential force in the clockwise direction is regarded as the positive force, where positive ones are plotted as filled symbols and negative ones are plotted as open symbols.

Even in our oscillatory shear system, the stress tensor $\sigma_{\alpha\beta}$ can be approximated as in Ref. [42]:

$$\sigma_{\alpha\beta}^* \simeq \sigma_{\alpha\beta}, \quad (20)$$

where we have introduced

$$\sigma_{\alpha\beta}^* := C \langle F_N \rangle \int_0^{2\pi} d\theta [\zeta_n(\theta) \mathbf{n}_\theta - \zeta_t(\theta) \mathbf{t}_\theta] \mathbf{n}_\theta^T \quad (21)$$

with a constant C determined by the relation $P = -(\sigma_{xx}^* + \sigma_{yy}^*)/2$. Here $\mathbf{n}_\theta = (\cos \theta, \sin \theta)$ and $\mathbf{t}_\theta =$

$(-\sin \theta, \cos \theta)$ are the normal and the tangential unit vectors between contacting grains, respectively. Figure 6 (a) plots the results of our simulation $\tilde{\sigma}$ and the theoretical expression $\tilde{\sigma}^*$ obtained from Eq. (21) by a parallel procedure to obtain $\tilde{\sigma}$. It is remarkable that the theoretical stress $\tilde{\sigma}^*$ well recovers $\tilde{\sigma}$ of our simulation at least, for $\gamma_{0,\text{eff}} \geq 0.1$. There exist some visible differences between the theoretical stress and the numerical stress for $\gamma_{0,\text{eff}} \leq 0.01$, but their qualitative shapes are almost identical. To demonstrate the relevancy of the theoretical expression Eq. (21) even for weakly non-linear region, $1.0 \times 10^{-3} < \gamma_{0,\text{eff}} \leq 0.1$, we have introduced the scaled stress $\tilde{\sigma}_{\text{fit}}^*$:

$$\tilde{\sigma}_{\text{fit}}^* := \frac{\tilde{\sigma}(\Omega t = \pi/2)}{\tilde{\sigma}^*(\Omega t = \pi/2)} \tilde{\sigma}^*(t). \quad (22)$$

It is obvious that $\tilde{\sigma}_{\text{fit}}^*$ recovers the most of the numerical results for $\gamma_{0,\text{eff}} \geq 1.0 \times 10^{-3}$. It should be noted that the Lissajous (the stress-strain) curve becomes an identical parallelogram for large $\gamma_{0,\text{eff}}$ as shown in Fig. 6. Because we reproduce the stress-strain curve via the phenomenology with the aid of $\zeta_n(\theta)$ and $\zeta_t(\theta)$, we can also reproduce G' and G'' via the phenomenological storage moduli G'_* and loss moduli G''_* (see the lines in Figs. 3 and 4), where $G'_* := \lim_{\gamma \rightarrow \gamma_{0,\text{eff}}} \tilde{\sigma}^*/\gamma_{0,\text{eff}}$ and $G''_* := \lim_{\gamma \rightarrow 0(\tilde{\sigma}^* \geq 0)} \tilde{\sigma}^*/\gamma_{0,\text{eff}}$.

We should note that the agreement between the phenomenology and the simulation is poor for small strain amplitudes. Disagreement of G'' for small $\gamma_{0,\text{eff}}$ is expected because we do not use Eq. (22) in Fig. 4. Note that we can reproduce the peak if we use Eq. (22) but the agreement of scaled one with the aid of Eq. (22) with the numerical one is still poor for small $\gamma_{0,\text{eff}}$. Nevertheless, we should emphasize that we capture the quantitative behavior of G' and G'' for the large strain amplitudes with the aid of the angular distribution function of the contact force. In this subsection, we have presented the results only for $\mu = 1.0$. In Appendix C we have discussed how the results of Eqs. (13)-(19) depend on μ . In the short summary of μ -dependence of the scaling laws presented in this subsection, (i) the scaling laws in Eqs. (13)-(19) still hold for arbitrary μ , and (ii) the exponent α''_μ depends on μ but the exponents β'_μ and β''_μ are almost independent of μ .

Influence of μ

In this subsection, we show how the results depend on the friction constant μ . Figure 7 plots the data of the storage modulus for various friction coefficients μ in cases of $P/k_n = 2.0 \times 10^{-4}$, $\Omega/(2\pi\sqrt{k_n/m_0}) = 1.0 \times 10^{-4}$. We recognize that the storage modulus are almost independent of μ if μ is finite, though the behavior of frictionless grains is quite different from those for frictional grains. It is not surprised that G' is essentially independent of μ because the scaling is only determined by the transient

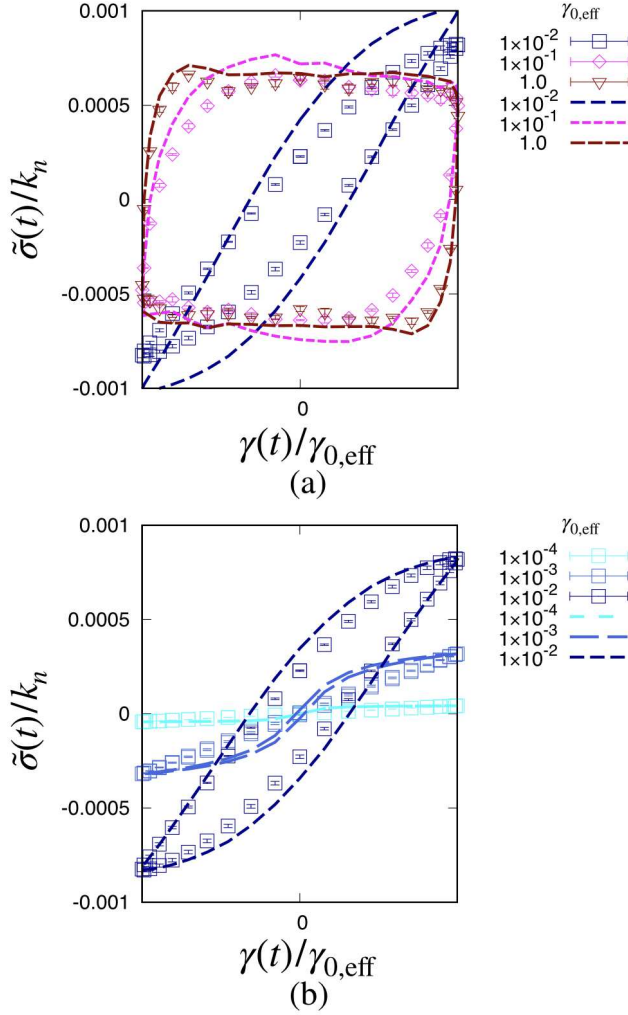


FIG. 6. Plots of Lissajous (stress-strain) curves for various $\gamma_{0,\text{eff}}$. (a) Numerical data $\tilde{\sigma}(t)$ are plotted by open symbols, and the theoretical stress $\tilde{\sigma}^*(t)$ with the aid of angular distributions for the normal contact force density $\zeta_n(\theta)$ and the tangential force density $\zeta_t(\theta)$ are plotted by the lines for large $\gamma_{0,\text{eff}}$. (b) Numerical data $\tilde{\sigma}(t)$ are plotted by open symbols and the theoretical stress $\tilde{\sigma}_{\text{fit}}^*$ with the aid of Eq. (22) are plotted by the lines for small $\gamma_{0,\text{eff}}$.

from the Hookean to the plastic regime ($G' \sim \gamma_{0,\text{eff}}^{-1}$), in which the friction constant does not appear in the argument to understand the scaling law.

On the other hand the loss modulus depends on the friction coefficient as

$$G'' = k_n \mu^{-\chi} \mathcal{F}'' \left(\frac{\gamma_{0,\text{eff}}}{\mu^\nu} \right). \quad (23)$$

Here, the scaling function satisfies the asymptotic forms:

$$\lim_{x \searrow 0} \mathcal{F}''(x) = \text{const.}, \quad \lim_{x \rightarrow \infty} \mathcal{F}''(x) \sim x^{-1}. \quad (24)$$

The scaling exponents used in Eq. (23) are evaluated as

$$\chi = 0.48, \quad \nu = 0.90. \quad (25)$$

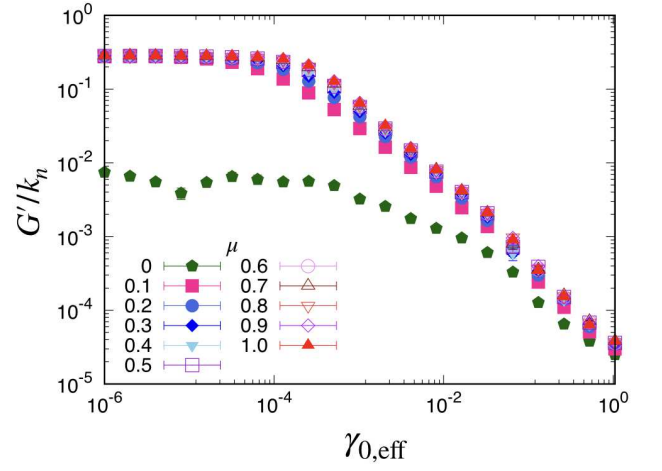


FIG. 7. Plots of the storage modulus against $\gamma_{0,\text{eff}}$ for various friction coefficients μ ranged from 0 to 1 at the pressure $P/k_n = 2.0 \times 10^{-4}$.

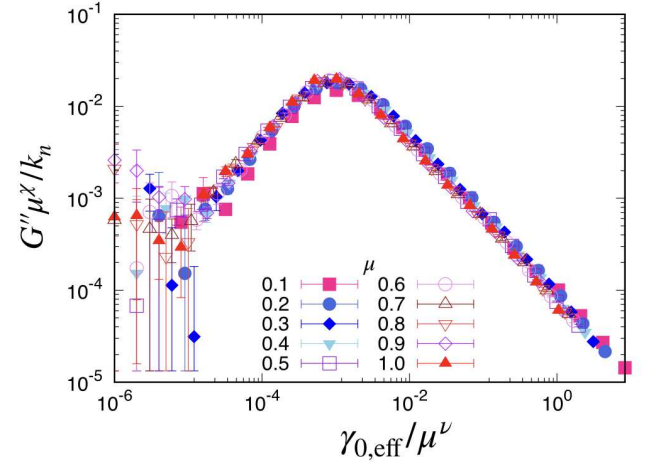


FIG. 8. The scaling plots of the loss modulus against $\gamma_{0,\text{eff}}$ for various μ at the pressure $P/k_n = 2.0 \times 10^{-4}$.

So far, we do not understand these scaling exponents for the loss modulus.

Although we present the data only for $P/k_n = 2.0 \times 10^{-4}$ in this subsection, as shown in Appendix , the scaling as in Eqs. (23) and (24) still hold in the other P , where the scaling exponents χ and ν little depend on P .

DILATANCY AND COMPACTION

Yielding transition

The yielding transition distinguishes an elastic and a reversible state for small strain from a plastic and an irreversible state for large strain. We regard the transition point as $\Delta x^2/d_0^2 = 1.0 \times 10^{-6}$ (see Fig. 9 (a)). We compare this definition with the violation of the Hookean

where $\hat{\sigma}$ is no longer proportional to $\gamma_{0,\text{eff}}$ (see Fig. 9 (b)). Here $\hat{\sigma}$ is given by

$$\hat{\sigma} = \frac{|\overline{\tilde{\sigma}}|}{\lim_{\gamma_{0,\text{eff}} \rightarrow 0} |\tilde{\sigma}|}, \quad (26)$$

where $|\overline{\tilde{\sigma}}|$ expresses the time average of $|\tilde{\sigma}|$ over one oscillation period. Thus, we confirm that the yielding point determined by $\Delta x^2/d_0^2 = 1.0 \times 10^{-6}$ is almost identical to the violation of the Hookean law for $P/k_n \leq 2.0 \times 10^{-4}$ (see the connected line among open triangles in Fig. 10).

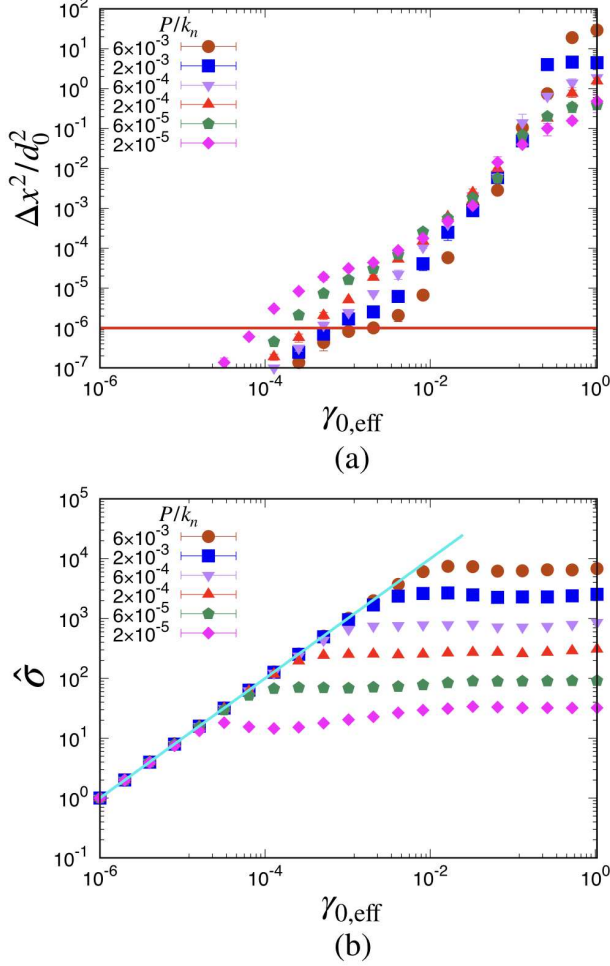


FIG. 9. (a) The mean square displacement Δx^2 versus the effective strain amplitude $\gamma_{0,\text{eff}}$. (b) The normalized shear stress $\hat{\sigma}$ defined in Eq. (26) versus $\gamma_{0,\text{eff}}$.

Dilatancy and compaction

As mentioned in INTRODUCTION, the dilatancy is one of the well known characteristics of granular flows. To characterize the dilatancy, we plot the data on the plane of the strain amplitude $\gamma_{0,\text{eff}}$ and the time averaged area fraction $\bar{\phi} := \int_0^T dt \phi(t)/T$ where ϕ is the area

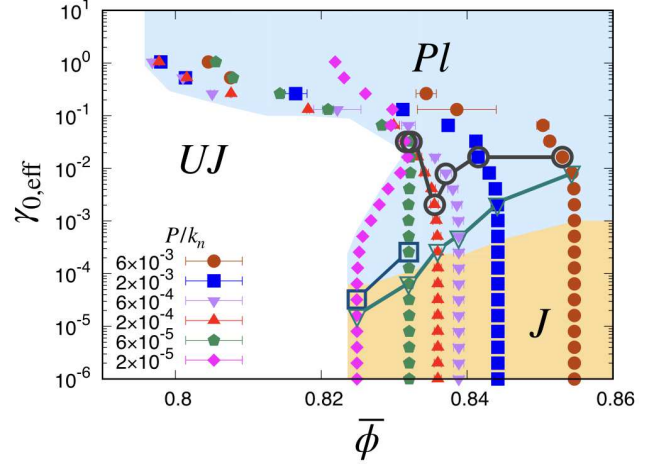


FIG. 10. The phase diagram spanned by the averaged area fraction $\bar{\phi}$ against $\gamma_{0,\text{eff}}$. The plastic region (Pl) is defined as $\Delta x^2 \geq 1.0 \times 10^{-6}$ and the jammed (J) state is defined as $\Delta x^2 < 1.0 \times 10^{-6}$. The points of the violation of the Hookean law, the first peaks of $\bar{\tau}$, and the last peak of $\bar{\tau}$ are plotted as open triangles, open squares and open circles, respectively.

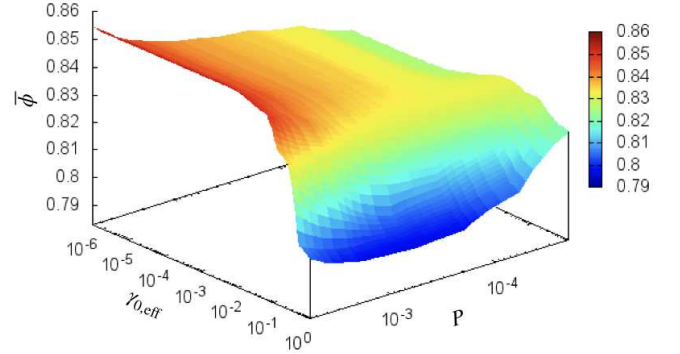


FIG. 11. Three-dimensional plot of $\bar{\phi}$ on the plane of $\gamma_{0,\text{eff}}$ and P , where the coding is a linear function of $\bar{\phi}$.

fraction in the bulk region (see Fig.10). Note that we cannot observe any unjammed phase because we always compress the system from the outside. It is remarkable that the compaction (instead of the dilatancy) takes place for $P/k_n \leq 6.0 \times 10^{-5}$ and the intermediate $\gamma_{0,\text{eff}}$ in which the density increases as strain increases. This compaction behavior is understood as the process from a random and metastable configuration to a stable and a little ordered configuration under the mild agitation. Such a compaction has been observed in a granular tapping process [51]. Figure 11 is the three-dimensional plot of the area fraction on the plane of P and $\gamma_{0,\text{eff}}$ to clarify the dilatancy and the compaction. It is interesting that the transition point of the compaction from the jammed phase in which the volume is unchanged is almost identical to that for the yielding pint determined by $\Delta x^2 \neq 0$. To characterize the dilatancy and the compaction we plot the av-

eraged stress anisotropy $\bar{\tau} := \int_0^T dt |\lambda_1 - \lambda_2| / (2T)$ in Fig. 12, where λ_1 and λ_2 are two eigenvalues of stress tensor. Note that the pressure is expressed as $P = -(\lambda_1 + \lambda_2)/2$. From comparison of Fig. 12 with Figs. 10 and 11, we can observe compaction for the intermediate $\gamma_{0,\text{eff}}$ between two peaks of $\bar{\tau}/P$, while there is no compaction if there is only a single peak for $\bar{\tau}/P$. The dilatancy can be only observed if $\gamma_{0,\text{eff}}$ is larger than that for the largest peak of $\bar{\tau}/P$. This characteristic behavior corresponds to the known fact that the anisotropy becomes largest in the fragile state [18, 24]. Furthermore, the peak of $\bar{\tau}/P$ at the dilatancy is sharper than that of the compaction. Thus, anisotropic structure plays important roles in the process of the dilatancy and the compaction.

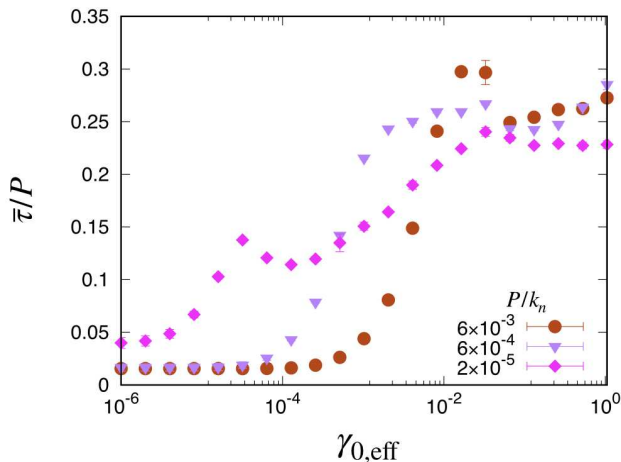


FIG. 12. Plots of $\bar{\tau}/P$ against $\gamma_{0,\text{eff}}$ for typical three pressures. The dilatancy and the compaction exist at $P/k_n = 2.0 \times 10^{-5}$ (diamonds). The dilatancy only exists at $P/k_n = 6.0 \times 10^{-4}$ (triangles) and $P/k_n = 6.0 \times 10^{-3}$ (circles).

DISCUSSION AND CONCLUSION

Let us discuss our results. The dilatancy law $\phi \propto \dot{\gamma} \sqrt{m/P}$ with the shear rate $\dot{\gamma}$ was reported for a two dimensional pressure control system under the steady shear [36, 42]. This simple law does not hold in our systems.

For large shear inter-grain collisions may play important roles. It is well known that the shear stress in high shear regime satisfies $\sigma \propto P$ for collisional frictionless and moderately dense granular gases [52]. Even for our systems, the shear stress satisfies the relation $\bar{\sigma} \propto P$ in the large strain amplitudes. The grains are stationary

for low strain regime while the motion of grains is irreversible to show the plasticity in the collisional regime. Quantitative analysis along this picture will be considered elsewhere.

We have verified that the phenomenology in terms of the angular distribution of the contact force gives quantitatively precise results for large strain amplitudes. Therefore, we will have to (i) construct the phenomenology for low strain amplitudes and (ii) try to derive the angular distribution of the contact force theoretically in future.

In summary, we have numerically investigated a frictional granular system confined by a constant pressure under an oscillatory shear. We found that the storage modulus satisfies $G'/G'_{\text{res}} = 1$ for small strain amplitudes (or high pressures) and $G'/G'_{\text{res}} \propto \hat{P}/\gamma_{0,\text{eff}}$ for large strain amplitudes (or small pressures). We have confirmed that G' is independent of μ while the loss modulus G'' satisfies a scaling law which depends on μ . The phenomenological theory with the aid of the angular distribution of the contact force works well, at least, for large strain amplitudes. We also found that the compaction in addition to the conventional dilatancy exists for the small pressure $P/k_n \leq 6.0 \times 10^{-5}$. The stress anisotropy takes a sharp peak at the critical point to start the dilatancy or the compaction.

ACKNOWLEDGEMENT

One of the authors (DI) expresses his sincere gratitude to T. G. Sano, S. Takada and K. Saitoh for their assists for the granular simulation. The authors thank M. Otsuki and T. Kawasaki for fruitful discussions. This work is partially supported by the the Grant-in-Aid of MEXT for Scientific Research (Grant No. 16H04025) and the Programs YITP-T-18-03 and YITP-W-18-1.

Angular frequency dependence

In this appendix, we check the dependence of the storage and the loss moduli on Ω . We have confirmed that G' and G'' are almost independent of Ω for $\Omega/(2\pi\sqrt{k_n/m_0}) \leq 1.0 \times 10^{-4}$, though the data of G'' in small $\gamma_{0,\text{eff}}$ are largely fluctuated (see Fig. 13).

Coupled stress and asymmetric stress

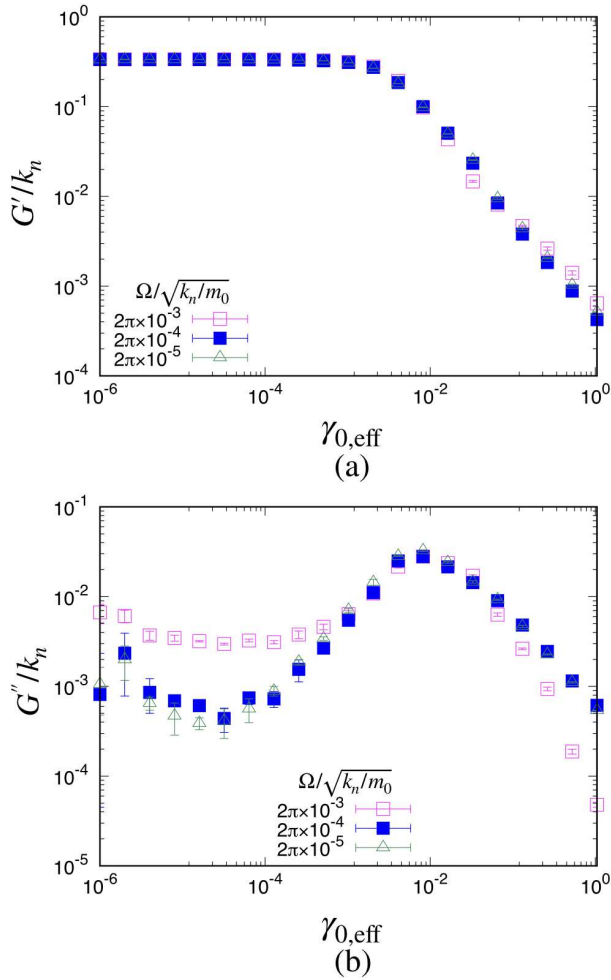


FIG. 13. Plots of G' and G'' against $\gamma_{0,\text{eff}}$ for various angular frequencies Ω at $P/k_n = 2.0 \times 10^{-3}$ and $\mu = 1.0$.

In this appendix, we discuss the coupled stress R which is the asymmetric part of the stress tensor [43] defined as

$$\begin{aligned}
 R &:= \frac{1}{L_x \tilde{L}_y} \sum_{\substack{i \\ (|y_i| < \tilde{L}_y/2)}} \sum_{j>i} (x_{ij,x} f_{ij,y} - x_{ij,y} f_{ij,x}), \\
 &= \frac{1}{L_x \tilde{L}_y} \sum_{\substack{i \\ (|y_i| < \tilde{L}_y/2)}} \sum_{j>i} T_{ij}.
 \end{aligned} \tag{1}$$

Let us introduce a normalized coupled stress \hat{R} :

$$\hat{R} := \frac{\tilde{R}}{\bar{\sigma}(\Omega t = \pi/4)}, \tag{2}$$

where $\tilde{R} := R - \int_0^T dt R/T$. We have confirmed the coupled stress is almost zero for large strain amplitudes as shown in Fig. 14. We find that \hat{R} depends on $\gamma(t)$ for the small pressure and small strain amplitudes. This behavior is reasonable because the couple stress is essentially the torque acting on grains. Although the contribution of $\hat{R}(t)$ for small strain amplitudes can be detected, the largest value of \hat{R} is at most 0.04. Therefore, we can safely ignore the contribution of asymmetric stress tensor or the couple stress.

Pressure dependence of G'_{res}

In this appendix, we discuss the behavior of $G'_{\text{res}} = \lim_{\gamma_{0,\text{eff}} \searrow 0} G'$ introduced in Eqs. (13) and (14). Figure

15 displays the results of our simulation on G'_{res} versus

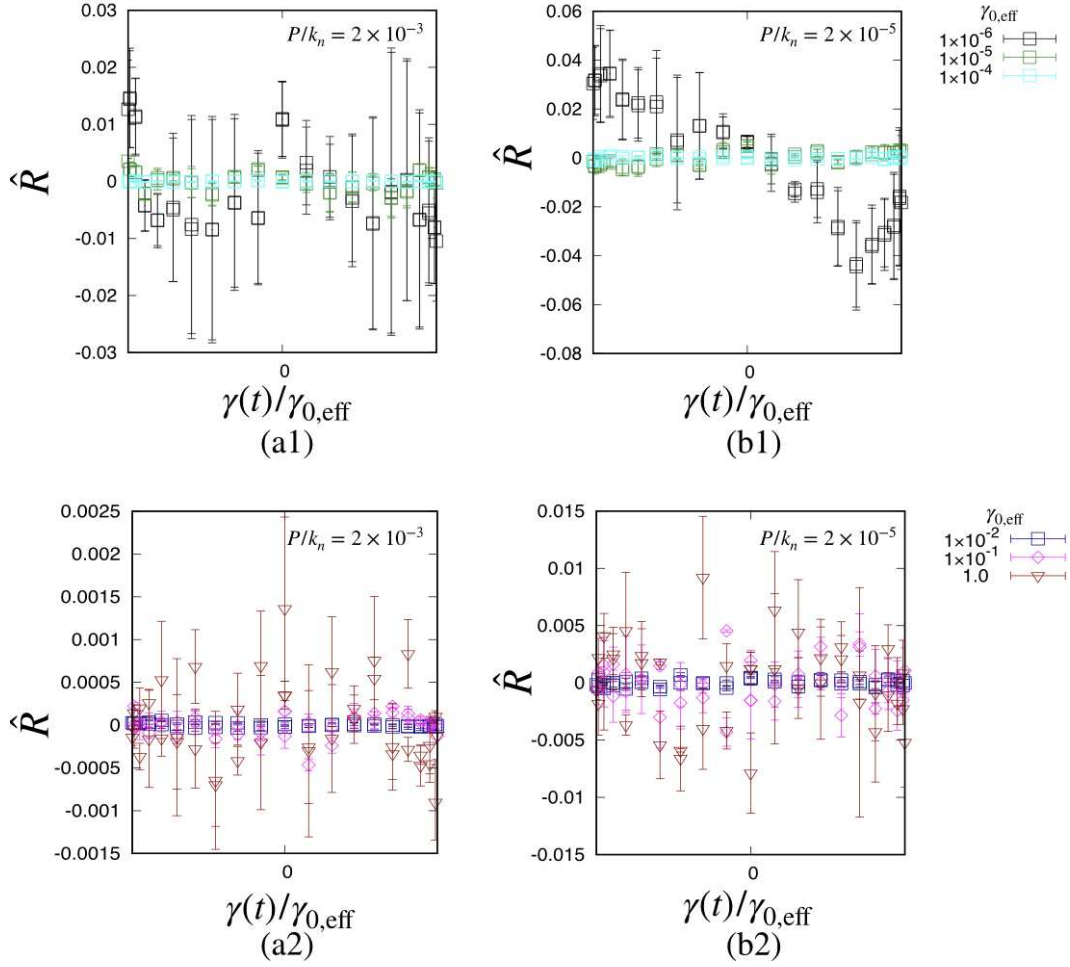


FIG. 14. Plots of \hat{R} against $\gamma(t)/\gamma_{0,\text{eff}}$ for (a1) $P/k_n = 2.0 \times 10^{-3}$ and small strain amplitudes, (a2) $P/k_n = 2.0 \times 10^{-3}$ and large strain amplitudes, (b1) $P/k_n = 2.0 \times 10^{-5}$ and small strain amplitudes and (b2) $P/k_n = 2.0 \times 10^{-5}$ and large strain amplitudes.

the external pressure P . Our results suggest that G'_{res} satisfies

$$\frac{G'_{\text{res}}}{k_n} \simeq a \log \hat{P} + b, \quad (3)$$

$$a = 0.03 \pm 0.01, \quad b = 0.49 \pm 0.01. \quad (4)$$

At present, we do not have any explanation of Eq. (3).

Scaling laws corresponding to Eqs. (13)-(19) for various friction coefficients

We have discussed the scaling laws in the main text (Sec.) only for $\mu = 1.0$. For arbitrary μ the storage modulus satisfies the relation:

$$G' = G'_{\text{res}}(\hat{P}) \mathcal{G}' \left(\frac{\gamma_{0,\text{eff}}}{\hat{P}^{\beta_\mu}} \right), \quad (5)$$

$$G'_{\text{res}}(\hat{P}) := \lim_{\gamma_{0,\text{eff}} \rightarrow 0} G'(\gamma_{0,\text{eff}}, \hat{P}) \quad (6)$$

$$\lim_{x \rightarrow 0} \mathcal{G}'(x) = 1, \quad \lim_{x \rightarrow \infty} \mathcal{G}'(x) \sim x^{-1}. \quad (7)$$

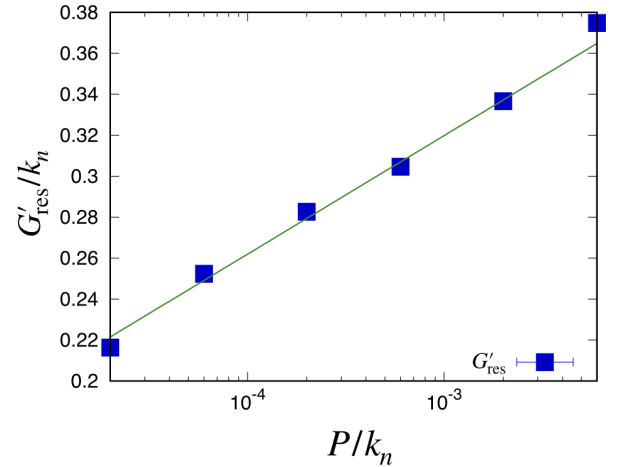


FIG. 15. Plot of G'_{res} against the pressure.

and the loss modulus satisfies the relation:

$$G'' = k_n \hat{P}^{\alpha''_\mu} \mathcal{G}'' \left(\frac{\gamma_{0,\text{eff}}}{\hat{P}^{\beta''_\mu}} \right), \quad (8)$$

$$\lim_{x \searrow 0} \mathcal{G}''(x) = \text{const.}, \quad \lim_{x \rightarrow \infty} \mathcal{G}''(x) \sim x^{-1}, \quad (9)$$

where the scaling exponents are plotted in Fig. 16. The

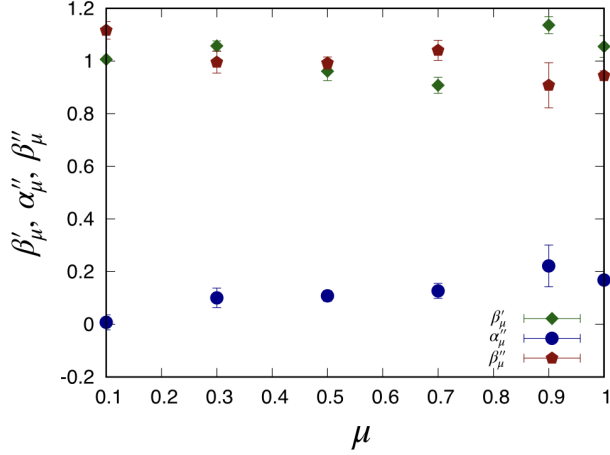


FIG. 16. Plots of β'_μ , α''_μ and β''_μ against μ .

exponents β'_μ and β''_μ are almost independent of μ , but α''_μ seems to depend on μ . See the scaling plots of G' and G'' against the scaled the strain amplitude in Fig. 17.

Scaling laws corresponding to Eqs. (23)-(25) for various pressures

We have confirmed that the loss modulus satisfies the scaling form only for $P/k_n = 2.0 \times 10^{-4}$ in the main text (Sec.). For arbitrary P the loss modulus may satisfy the scaling form:

$$G'' = k_n \mu^{-\chi_r} \mathcal{F}'' \left(\frac{\gamma_{0,\text{eff}}}{\mu^{\nu_r}} \right) \quad (r = s, m, l). \quad (10)$$

Here, the scaling function satisfies the asymptotic forms:

$$\lim_{x \searrow 0} \mathcal{F}''(x) = \text{const.}, \quad \lim_{x \rightarrow \infty} \mathcal{F}''(x) \sim x^{-1} \quad (11)$$

where subscripts s , m , l correspond to $P/k_n = 2.0 \times 10^{-5}$, $P/k_n = 2.0 \times 10^{-4}$, $P/k_n = 2.0 \times 10^{-3}$, respectively. We find that the best fitted scaling exponents used in Eq. (10) are given by

$$\chi_s = 0.46, \quad \nu_s = 0.80, \quad (12)$$

$$\chi_m = 0.48, \quad \nu_m = 0.90, \quad (13)$$

$$\chi_l = 0.46, \quad \nu_l = 0.90. \quad (14)$$

It seems that the exponents χ_r and ν_r little depend on P . The scaling plot of the loss modulus based on Eq. (10) for $P/k_n = 2.0 \times 10^{-5}$ is shown in Fig. 18.

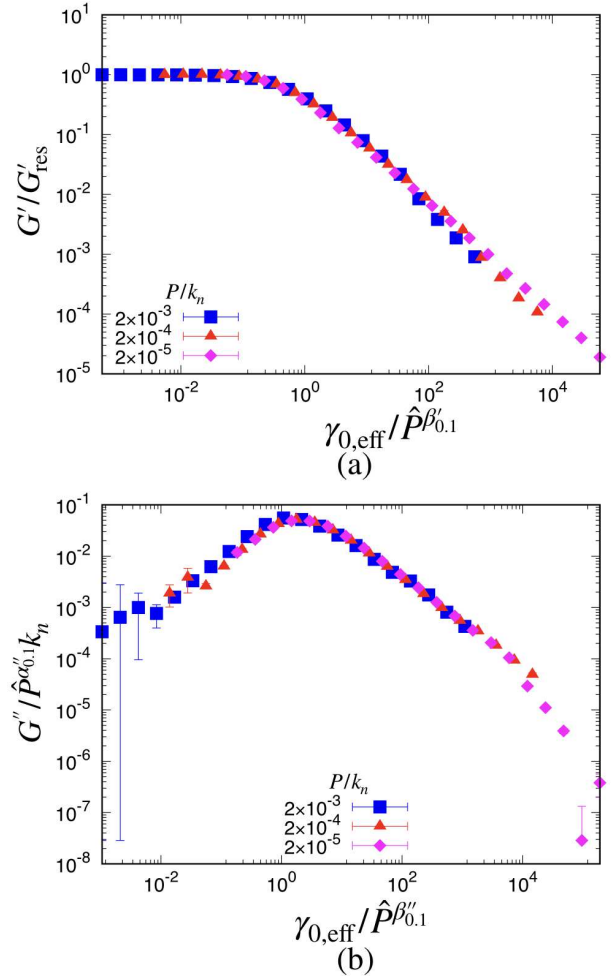


FIG. 17. Scaling plots of G' and G'' against the scaled the strain amplitude for various dimensionless pressures \hat{P} at $\mu = 0.1$

-
- [1] H. M. Jaeger, S. R. Nagel, and R. P. Behringer, Rev. Mod. Phys. **68**, 1259 (1996).
 - [2] P. N. Pusey, in Liquids, Freezing and the Glass Transition, Part II, Les Houches Summer School Proceedings Vol. 51, edited by J.-P. Hansen, D. Levesque, and J. Zinn-Justin (Elsevier, Amsterdam, 1991), Chap. 10.
 - [3] D. J. Durian and D. A. Weitz, in Foams, in Kirk-Othmer Encyclopedia of Chemical Technology, 4th ed., edited by J. I. Kroschwitz (Wiley, New York, 1994), Vol. 11, p. 783.
 - [4] A. J. Liu and S. R. Nagel, Nature **396**, 21 (1998).
 - [5] C. S. O'Hern, L. E. Silbert, A. J. Liu and S. R. Nagel, Phys. Rev. E **68**, 011306 (2003).
 - [6] V. Trappe, V. Prasad, L. Cipelletti, P. N. Segre and D. A. Weitz, Nature **411**, 772 (2001).
 - [7] T. S. Majmudar, M. Sperl, S. Luding, and R. P. Behringer, Phys. Rev. Lett **98**, 058001 (2007).
 - [8] W. G. Ellenbroek, E. Somfai, M. van Hecke and W. van Saarloos, Phys. Rev. Lett. **97**, 258001 (2006).
 - [9] P. Olsson and S. Teitel, Phys. Rev. Lett. **99**, 178001 (2007).
 - [10] T. Hatano, J. Phys. Soc. Jpn. **77**, 123002 (2008).

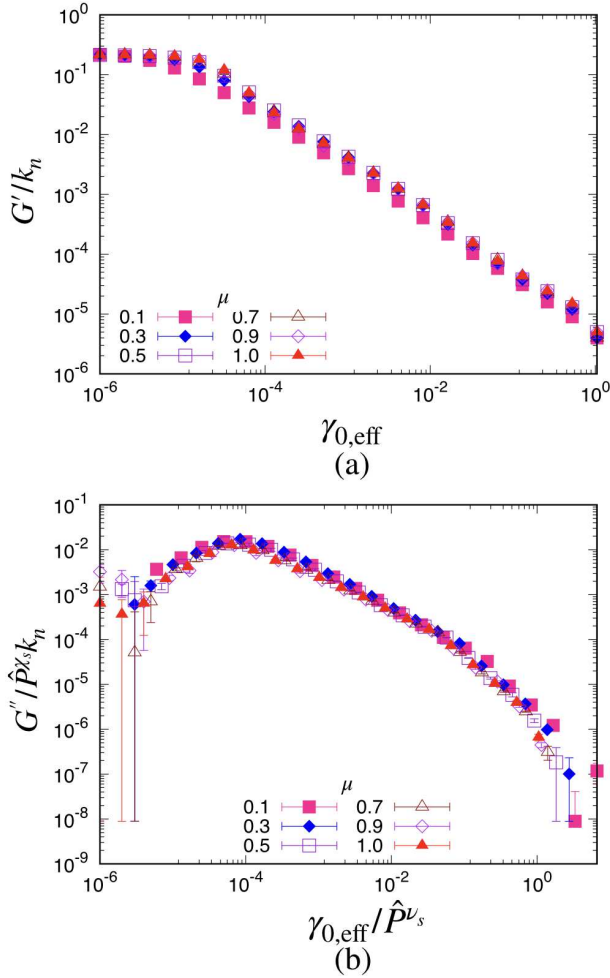


FIG. 18. (a) Plots of G' and (b) the scaling plots of G'' for various friction coefficients at $P/k_n = 2.0 \times 10^{-5}$.

[11] M. Otsuki and H. Hayakawa, Phys. Rev. E **80**, 011308 (2009).
 [12] E. Brown and H. M. Jaeger, Phys. Rev. Lett. **103**, 086001 (2009).
 [13] M. Otsuki and H. Hayakawa, Phys. Rev. E **83**, 051301 (2011).
 [14] R. Seto, R. Mari, J. F. Morris, and M. M. Denn, Phys. Rev. Lett. **111**, 218301 (2013).
 [15] M. Wyart and M. E. Cates, Phys. Rev. Lett. **112**, 098302 (2014).
 [16] M. Otsuki and H. Hayakawa, Phys. Rev. E **95**, 062902 (2017).
 [17] T. Kawasaki and L. Berthier, Phys. Rev. E **98**, 012609 (2018).
 [18] D. Bi, J. Zhang, B. Chakraborty and R. Behringer, Nature **480**, 355 (2011).
 [19] J. Zhang, T. S. Majmudar and R. Behringer, Chaos **18**, 041107 (2008).
 [20] J. Zhang, T. S. Majmudar, A. Tordesillas and R. P. Behringer, Granul. Matt. **12**, 159 (2010).
 [21] D. Wang, J. Ren, J. A. Dijksman, H. Zheng and R. P. Behringer, Phys. Rev. Lett. **120**, 208004 (2018).

[22] S. Sarkar, D. Bi, J. Zhang, R. P. Behringer and B. Chakraborty, Phys. Rev. Lett. **111**, 068301 (2013).
 [23] S. Sarkar, D. Bi, J. Zhang, J. Ren, R. P. Behringer and B. Chakraborty, Phys. Rev. E **93**, 042901 (2016).
 [24] M. Otsuki and H. Hayakawa, arXiv:1810.03846.
 [25] A. Fall, F. Bertrand, D. Hautemayou, C. Mezière, P. Moucheront, A. Lemaitre and G. Ovarlez, Phys. Rev. Lett. **114**, 098301 (2015).
 [26] I. R. Peters, S. Majumdar and H. M. Jaeger, Nature **532**, 214 (2016).
 [27] P. Hébraud, F. Lequeux, J. P. Munch and D. J. Pine, Phys. Rev. Lett., **78**, 4657 (1997).
 [28] D. Fiocco, G. Foffi and S. Sastry, Phys. Rev. E **88**, 020301 (2013).
 [29] A. H. Clark, J. D. Thompson, M. D. Shattuck, N. T. Ouellette and C. S. O'Hern, Phys. Rev. E **97**, 062901 (2018).
 [30] G. Petekidis, A. Moussaïd and P. N. Pusey, Phys. Rev. E **66**, 051402 (2002).
 [31] J. Lin, E. Lerner, A. Rosso and M. Wyart, Proc. Natl. Acad. Sci. U.S.A. **111**, 14382 (2014).
 [32] T. Kawasaki and L. Berthier, Phys. Rev. E **94**, 022615 (2016).
 [33] O. Reynolds, Philos. Mag. Ser. **20**, 469 (1885).
 [34] P. A. Thompson and G. S. Grest, Phys. Rev. Lett. **67**, 1751 (1991).
 [35] J. H. Snoeijer, T. J. H. Vlugt, M. van Hecke and W. van Saarloos, Phys. Rev. Lett. **92**, 054302 (2004).
 [36] Y. Forterre and O. Pouliquen, Annu. Rev. Fluid Mech. **40**, 1 (2008).
 [37] F. Boyer, É. Guazzelli and O. Pouliquen, Phys. Rev. Lett. **107**, 188301 (2011).
 [38] S. Luding, Phys. Rev. E **63**, 042201 (2001).
 [39] P. A. Cundall and O. D. L. Strack, Geotechnique **29**, 47 (1979).
 [40] S. Luding, Granul. Matt. **10**, 235 (2008).
 [41] J. J. Moreau, in Friction, Arching, Contact Dynamics, edited by D. E. Wolf and P. Grassberger (World Scientific, London, 1997), pp. 233-247.
 [42] F. da Cruz, S. Emam, M. Prochnow, J. Roux and F. Chevoir, Phys. Rev. E **72**, 021309 (2005).
 [43] I. Goldhirsch, Granul. Matt. **12**, 239 (2010).
 [44] M. Doi and F. Edwards, The Theory of Polymer Dynamics (Oxford Univ. Press, 1986).
 [45] R. H. Ewoldt, A. E. Hosoi and G. H. McKinley, J. Rheol. **52**, 1427 (2008).
 [46] R. I. Argatov, A. Iantchenko and V. Kochebitov, Contin. Mech. Thermodyn. **29**, 1375 (2017).
 [47] K. Hyun, M. Wilhelm, C. O. Klein, K. S. Cho, J. G. Nam, K. H. Ahn, S. J. Lee, R. H. Ewoldt and G. H. McKinley, Prog. Polym. Sci. **36**, 1697 (2011).
 [48] F. Calvetti, G. Combe and J. Lanier, Mech. Cohesive-Frict. Mater. **2**, 121 (1997).
 [49] K. Kanatani, Powder Technol. **28**, 167 (1981).
 [50] B. Cambou, P. Dubujet, F. Emeriault and F. Sidoroff, Eur. J. Mech. A/Solids **14**, 255 (1995).
 [51] E. R. Nowak, J. B. Knight, E. Ben-Naim, H. M. Jaeger and S. R. Nagel, Phys. Rev. E **57**, 1971 (1998).
 [52] H. Hayakawa, S. Takada and V. Garzó, Phys. Rev. E **96**, 042903 (2017).